Electrical Modulation and Probing of Antiferromagnetism in Hybrid Multiferroic Heterostructures

Yuhan Liang,[1,2,*] Huiping Han,[3,*] Hetian Chen,[1,*] Yujun Zhang,[4] Yi Zhang,[3] Chao Li,[1] Shun Lan,[1] Fangyuan Zhu,[5] Ji Ma,[3] Di Yi,[1] Jing Ma,[1] Liang Wu,[3,†] Tianxiang Nan,[2,‡] and Yuan-Hua Lin[1,§]

[1] *School of Materials Science and Engineering, Tsinghua University, Beijing, 100084, People's Republic of China*
[2] *School of Integrated Circuits and Beijing National Research Center for Information Science and Technology (BNRist), Tsinghua University, Beijing 100084, China*
[3] *Faculty of Materials Science and Engineering, Kunming University of Science and Technology, Kunming, Yunnan 650093, People's Republic of China*
[4] *Institute of High Energy Physics, Chinese Academy of Sciences, Beijing 100049, People's Republic of China*
[5] *Shanghai Synchrotron Radiation Facility, Shanghai Advanced Research Institute, Chinese Academy of Sciences, Shanghai 201204, People's Republic of China*

(Dated: November 21, 2025)

The unique features of ultrafast spin dynamics and the absence of macroscopic magnetization in antiferromagnetic (AFM) materials provide a distinct route towards high-speed magnetic storage devices with low energy consumption and high integration density. However, these advantages also introduce challenges in probing and controlling AFM order, thereby restricting their practical applications. In this study, we demonstrate an all-electric control and probing of the AFM order in heavy metal (HM)/AFM insulator (AFMI) heterostructures on a ferroelectric substrate at room temperature (RT). The AFM order was detected by the anomalous Hall effect (AHE) and manipulated by the ferroelectric field effect as well as the piezoelectric effect in heterostructures of Pt/NiO/0.7Pb($Mg_{1/3}Nb_{2/3}$)O_3–0.3$PbTiO_3$ (PMN–PT). The non-volatile control of AFM order gives rise to a 33% modulation of AHE, which is further evidenced by synchrotron-based X-ray magnetic linear dichroism (XMLD). Combined with the *in-situ* piezoelectric response of AHE, we demonstrate that ferroelectric polarization contributes mainly to the control of the AFM order. Our results are expected to have broader implications for efficient spintronic devices.

I. INTRODUCTION

Antiferromagnets (AFM) possess distinctive properties, such as ultrafast spin dynamics and the absence of macroscopic magnetization, making them promising candidates for the development of future spintronic devices [1–5]. Using the interaction between AFM order and itinerant electrons to detect AFM structures has attracted extensive attention [6–9]. A non-trivial AFM order, such as noncollinear AFM or altermagnetism, can break the time-reversal symmetry (TRS) and generate intrinsic Berry curvature, resulting in a transverse Hall field to deflect spin-polarized electrons and yielding the AHE [2, 7, 10–15]. Thus, detecting AHE in AFM materials indicates the presence of a non-trivial AFM order, which can be manipulated by the electric field effect [16, 17], piezoelectric strain [18, 19] or spin current [20, 21]. As numerous bulk AFM insulators (AFMI) host collinear AFM order (rather than altermagnetism) that protects TRS [1], most studies concentrate on metallic materials with non-trivial AFM order for magnetic memories [20, 22–25].

Recent advances show that a significant AHE around room temperature (RT) can also be observed in heterostructures comprising of AFMI and heavy metal (HM), which can be ascribed to the subtle interaction between spin current and non-trivial AFM structures during AFM–paramagnetic (AFM–PM) transition in HM/AFMI heterostructures [26–29]. The AFM–PM transition temperature (T_N) can be regarded as the competition between AFM exchange coupling strength (J_{ex}) and thermal fluctuation, in which the J_{ex} is sensitive to the lattice parameter and boundary condition [30]. Thus, in HM/AFMI heterostructures, the AFM order and correlated Berry curvature can be modulated by piezoelectric strain or ferroelectric field effect, which can be probed by AHE.

In this work, we demonstrate the electric-field control of AFM order probed by AHE in a hybrid HM/AFMI heterostructure on the piezoelectric substrate at RT. By depositing Pt/NiO heterostructures on a piezoelectric PMN–PT substrate and applying an *in-situ* electric field gating (E_{gate}), we observed a non-volatile modulation of AHE conductivity of about 33%. Through synchrotron-based X-ray magnetic linear dichroism (XMLD) measurements, we confirmed the non-volatile modulation of AFM order in NiO that correlated to the control AHE in HM/AFMI heterostructure. Further detailed analysis on piezoelectric strain and *in-situ* electric-field gating experiments indicates that the ferroelectric polarization field effect significantly dominates the control of AFM order. Our findings may facilitate the development of spintronic devices based on AFMIs.

* These authors contributed equally.
† liangwu@kust.edu.cn
‡ nantianxiang@mail.tsinghua.edu.cn
§ linyh@tsinghua.edu.cn

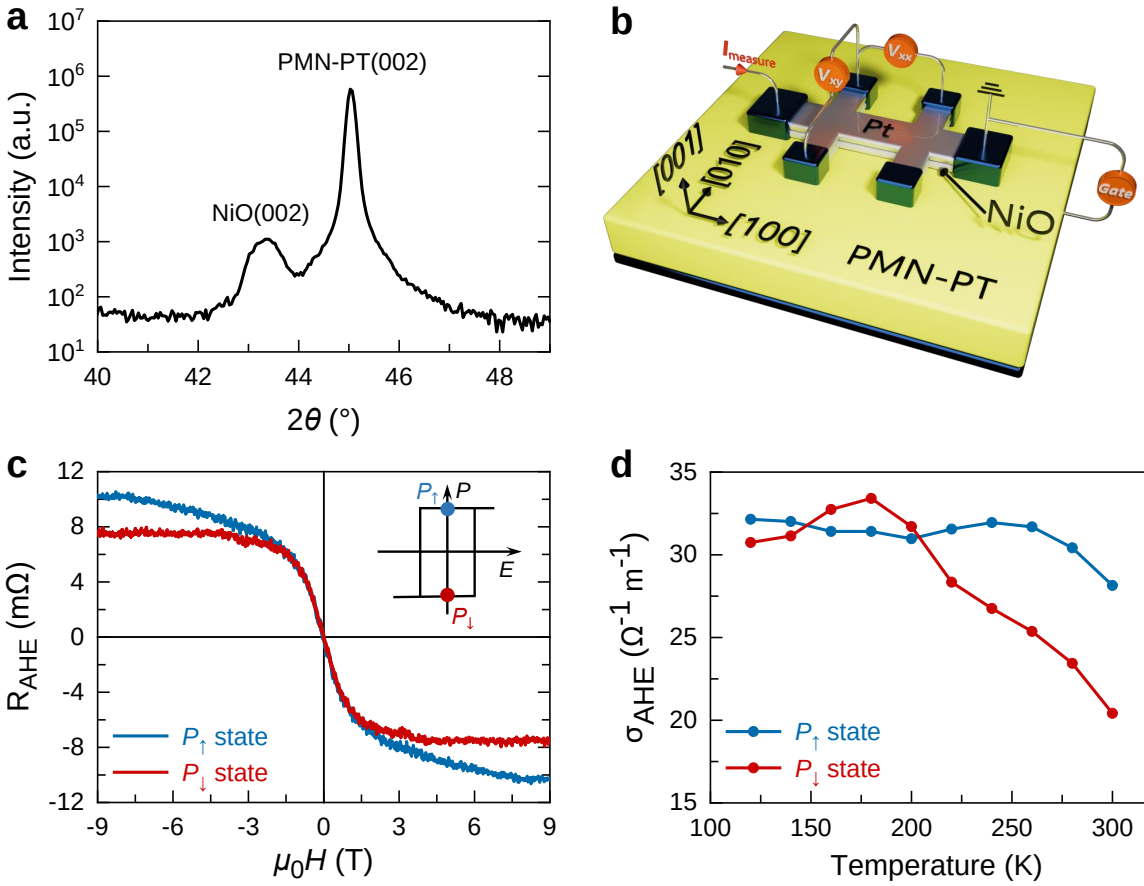

Figure 1. The non-volatile electric-field control of AHE in HM/AFMI heterostructure. (a) The zoomed XRD pattern around (002) peak of 20 nm NiO thin film on PMN–PT substrate. (b) The schematic diagram of Hall bar device and transport property measurement set-up of Pt(3 nm)/NiO(3 u.c.)/PMN–PT. (c) The non-volatile electric field control of $R_{\rm AHE}$ of Pt(3 nm)/NiO(3 u.c.)/PMN–PT for $P_{\uparrow}$ and $P_{\downarrow}$ states. The inset is schematic of polarization-electric field hysteresis loop. The blue and red dots represent the $P_{\uparrow}$ and $P_{\downarrow}$ states, respectively. (d) The temperature dependent $\sigma_{\rm AHE}$ of Pt(3 nm)/NiO(3 u.c.)/PMN–PT for $P_{\uparrow}$ and $P_{\downarrow}$ states.

II. RESULTS AND DISCUSSION

The epitaxial NiO layer was deposited on (001)-oriented piezoelectric PMN–PT substrates by pulsed laser deposition (PLD) with a 248 nm KrF excimer laser. The NiO growth was deposited with 700 °C substrate temperature and 4 Pa oxygen pressure. The corresponding pulse repetition was 5 Hz. After PLD deposition, the NiO/PMN–PT heterostructures were cooled to RT in an oxygen-rich atmosphere and then transferred to a magnetron sputtering chamber with a base vacuum better than 2×10^{-8} Torr. The Pt was sputter deposited with an Ar pressure of 3 mTorr. The Pt/NiO/PMN–PT(001) heterostructure was fabricated into Hall bars with 20 μm width and 50 μm distance between electrode leads using standard photolithography and ion milling processes. The 100 nm Pt/5 nm Ti bilayer was then deposited through magnetron sputtering for electrode contact. The epitaxy quality is characterized by using a high-resolution X-ray diffractometer (XRD), and the thickness of films was characterized by X-ray reflectivity (XRR) (see details in Figure S1 in Supplementary Materials). The sample surface morphology was characterized through atomic force microscopy. The electric field is applied through Keithley 2450 source-meter with silver paste on the PMN–PT substrate bottom as a back gating electrode. The transport property measurements were conducted in the Physical Property Measurement System (PPMS). The AHE and resistivity measurements were conducted after 20 minutes stabilization of the electric field. The ferroelectric property of PMN–PT substrate was monitored through a ferroelectric analyzer. The synchrotron-based XMLD was conducted in BL07U at Shanghai Synchrotron Radiation Facility (SSRF) with total yield electron (TEY) mode [31].

The zoomed XRD pattern around the (002) diffraction peak of PMN–PT(001) substrate shows the high epitaxy quality of 20 nm NiO thin film, as shown in Figure 1(a). We then decreased the thickness of NiO film and fabricated Pt(3 nm)/NiO(3 u.c.)/PMN–PT(001) heterostructure (u.c. is the abbreviation of unit cells), in which the

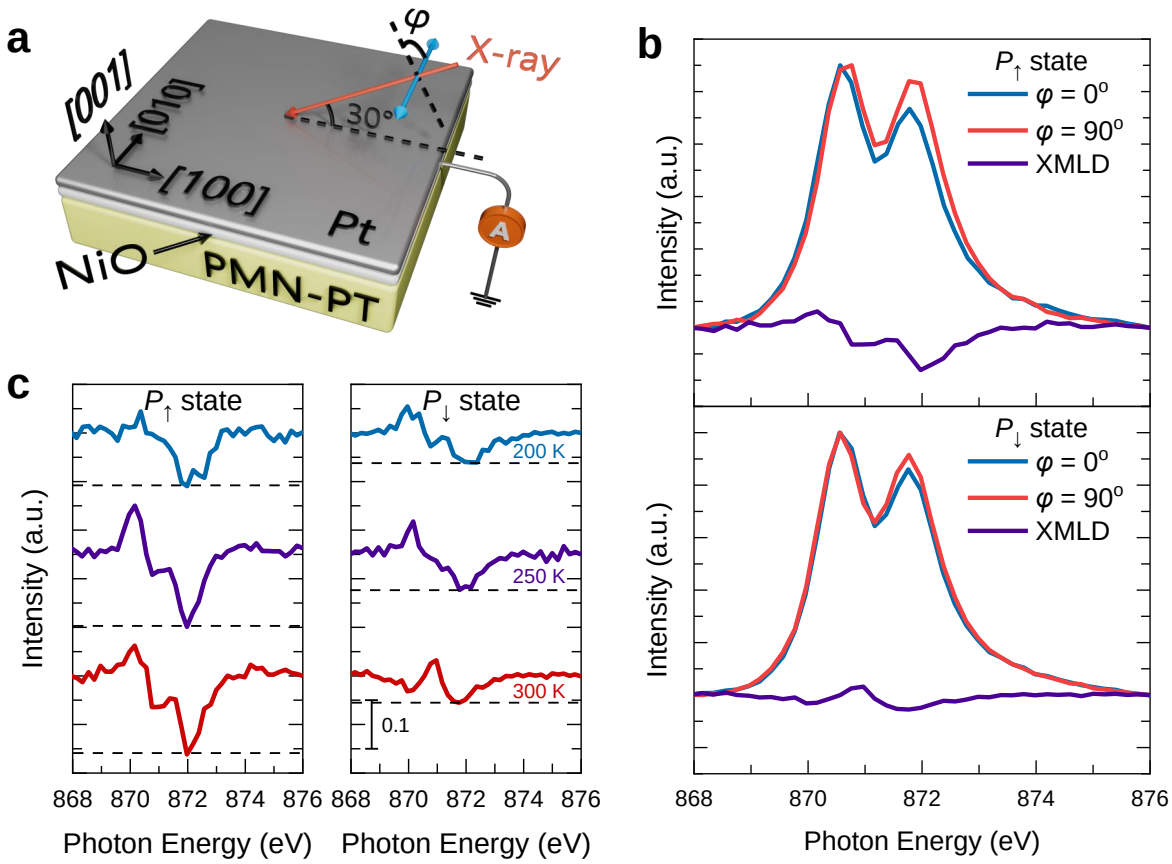

Figure 2. The synchrotron-based XAS and XMLD results of Pt(3 nm)/NiO(3 u.c.)/PMN–PT heterostructure. (a) The schematic diagram of XAS measurements set-up. (b) The XAS results for $P_\uparrow$ and $P_\downarrow$ states with $\varphi = 0°$ and $\varphi = 90°$, as well as corresponding XMLD results. (c) The temperature-dependent XMLD results for $P_\uparrow$ state and $P_\downarrow$ state, respectively. The dashed line denotes the peak amplitude of XMLD signal.

AFM–PM transition is around RT [26]. The surface morphology of Pt(3 nm)/NiO(3 u.c.)/PMN–PT(001) heterostructure is shown in Figure S2, Supplementary Materials, revealing a roughness of about 700 pm. The AHE and resistivity measurements were then conducted in a Hall bar device with measurement current I_{measure} of 0.5 mA applied along the in-plane [100] direction, corresponding to a current density of about 8.3×10^5 A/cm^2 about two orders lower than the value for substaintial spin-orbit torque effects [32, 33], as schematically shown in Figure 1(b). By applying $E_{\text{gate}} = \pm4$ kV/cm, the PMN–PT substrate can be poled into opposite ferroelectric polarization P. This electric field is homogeneously out-of-plane, minimizing the possible spin accumulation induced by in-plane electric field [34]. After poling of the PMN–PT substrate, the E_{gate} was removed and PMN–PT substrate relaxed into two remnant states with ferroelectric polarization about ±20 μC/cm^2 (noted as states $P_\uparrow$ and $P_\downarrow$, respectively), see polarization-electric field hysteresis loop in Figure S3, Supplementary Materials. The resistivity variation of the device was confirmed to be less than 0.4% between $P_\uparrow$ and $P_\downarrow$ states, as shown in Figure S4, Supplementary Materials. The AHE resistance R_{AHE} was monitored by sweeping the out-of-plane external magnetic field $\mu_0 H$ at RT for the states $P_\uparrow$ and $P_\downarrow$, as shown in Figure 1(c). It should be noted that the Hall data is an odd function as the sweeping magnetic field, avoiding the mixing of magnetoresistance, which is an even function. The ordinary Hall effect background induced by Lorentz force has been subtracted with coefficient about $3.7\times10^{-7}\,\Omega\,\text{Oe}^{-1}$ for the states $P_\uparrow$ and $3.6\times10^{-7}\,\Omega\,\text{Oe}^{-1}$ for the states $P_\downarrow$, respectively (see Figure S5 in Supplementary Materials for the raw Hall resistance results). It clearly shows the non-volatile electric-field control of AHE, as the saturated R_{AHE} for $P_\uparrow$ and $P_\downarrow$ states is 7.5 mΩ and 10 mΩ, respectively.

Considering the R_{AHE} originates from the combination between AHE conductance σ_{AHE} and longitudinal resistivity ρ_{xx}, we measured the ρ_{xx} of two remnant states and estimated the corresponded σ_{AHE} at various temperatures according to $\sigma_{\text{AHE}} = \rho_{\text{AHE}}/(\rho_{\text{AHE}}^2 + \rho_{xx}^2)$, where $\rho_{\text{AHE}} = R_{\text{AHE}}t$ and $t = 3$ nm is the thickness of the Pt layer. See detailed data on temperature-dependent AHE results in Figure S6, Supplementary Materials. The calculated σ_{AHE} are shown in Figure 1(d). At RT, the σ_{AHE} for the $P_\uparrow$ and $P_\downarrow$ states is approximately 28 and 20 Ω^{-1} m^{-1}, respectively, corresponding to 33% modulation of σ_{AHE} at RT. In the whole temperature range

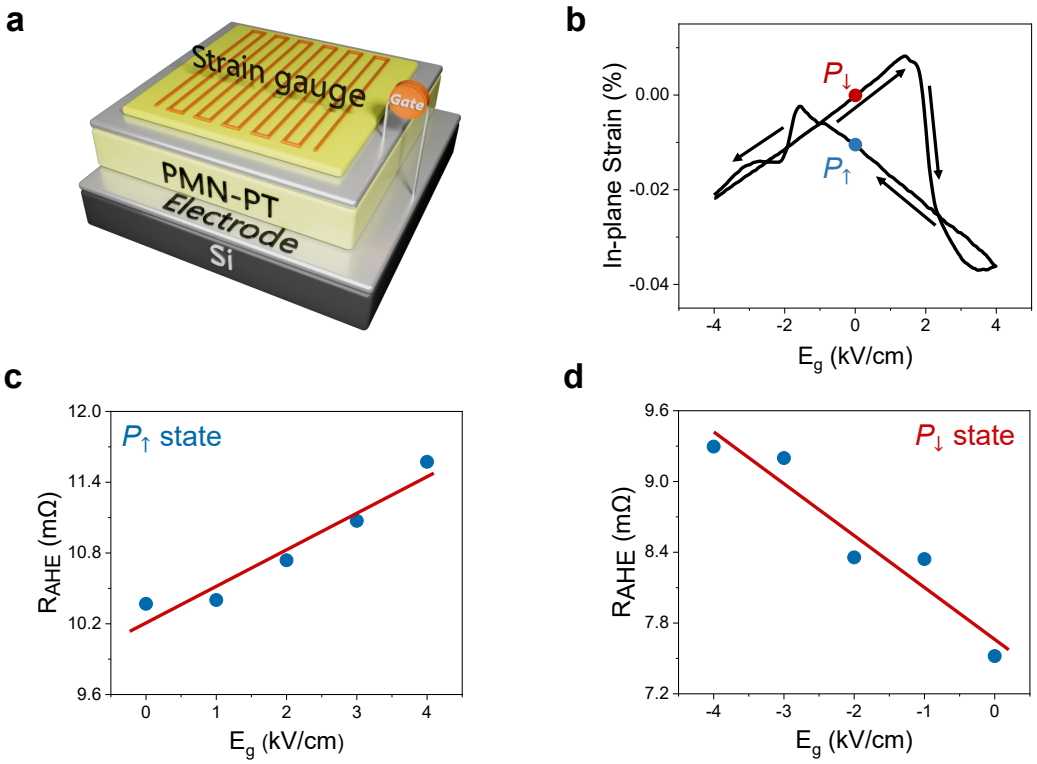

Figure 3. The piezoelectric effect on the AHE of Pt(3 nm)/NiO(3 u.c.)/PMN–PT heterostructure. (a) The schematic of measuring in-plane strain by strain gauge. (b) The monitored in-plane strain by sweeping out-of-plane electric field. The arrows indicate the sweeping direction of electric field. The blue and red dots represent the $P_{\uparrow}$ and $P_{\downarrow}$ states, respectively. (c) and (d), The electric-field dependent R_{AHE} for heterostructure with (c) $P_{\uparrow}$ and (d) $P_{\uparrow}$ states, respectively. The red lines indicate the linear fitting.

from 300 to 120 K, for $P_{\uparrow}$ state, a local maximum value of σ_{AHE} approximately 32 Ω^{-1} m^{-1} is observed around 240 K, while a local maximum value of 33 Ω^{-1} m^{-1} is observed around 180 K for $P_{\downarrow}$ state. These results suggest that the AFM strength of ultrathin NiO films is effectively modulated by E_{gate}.

To confirm the modulation of the AFM strength of ultrathin NiO film by E_{gate}, we utilized synchrotron-based XMLD measurements at the Ni L_2 edge using the same method described in Refs. [30, 35]. The experimental set-up is schematically shown in Figure 2(a), as the X-ray is incident in (010) plane with an angle of 30° with respect to the sample surface. The polarization vector $\vec{E}$ of X-ray can be modulated with angle φ ($\varphi = 0°$ or 90°) to the (010) plane. The L_2 intensity ratio in the X-ray absorption spectrum (XAS) at the Ni L_2 edge, defined as the ratio of the lower to higher energy peak intensities, is affected by the alignment of $\vec{E}$ with the Ni^{2+} spin easy axis [36] and exhibits linear dichroism. The linear dichroism effect can arise from the XMLD effect due to AFM order and the crystal field effect; however, the latter can be disregarded since our observations show an insignificant peak energy shift at the L_3 edge (see Figure S7 in Supplementary Materials), which also exclude the Ni defects in Pt (see Figure S8 in Supplementary Materials). By varying the angle φ, the L_2 intensity ratio of the normalized XAS signal could change and show the XMLD effect, which indicates the AFM order strength [30]. In this work, we define the XMLD signal = XAS($\varphi = 0°$) − XAS($\varphi = 90°$). The typical normalized XAS results with $\varphi = 0°$ and $\varphi = 90°$ and the corresponding XMLD signal for $P_{\uparrow}$ and $P_{\downarrow}$ states are shown in Figure 2(b) and Figure 2(c), respectively. For both states, the L_2 higher energy peak intensity always reaches its maximum value (or the minimum L_2 intensity ratio) with $\varphi = 90°$, indicating the Ni^{2+} spin easy axis lying in the sample plane and consistent with the reported easy-plane AFM structure of NiO thin film [37–39].

Then we utilized the XMLD signal to reveal the AFM order strength modulated by E_{gate}. The XMLD is significant for $P_{\uparrow}$ state, while it becomes weaker for $P_{\downarrow}$ state at 300 K, see Figure 2(b), supporting our previous demonstration of the non-volatile modulation on AFM order strength by E_{gate} according to AHE measurements in Figure 1. In addition, we also conducted XAS measurements with temperatures ranging from 300 K to 200 K, and obtained temperature-dependent XMLD results, as shown in Figure 2(c). For $P_{\uparrow}$ state, the XMLD signal remains significant as temperature decreases from 300 K to 200 K. We note that the XMLD signal shows a non-monotonic trend, as it becomes relatively weaker at 200 K than at 250 K, which can be ascribed to the AFM spin

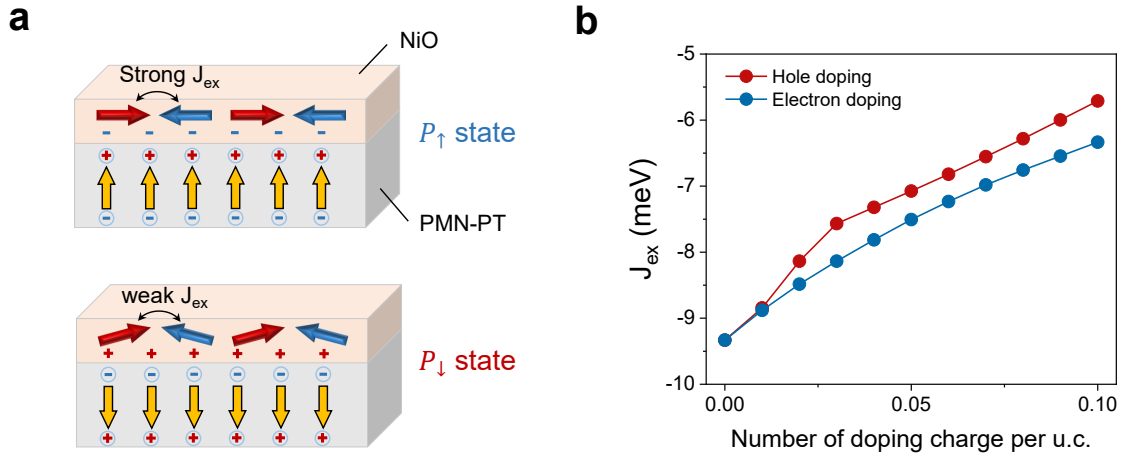

Figure 4. The DFT calculation of J_{ex} controlled by ferroelectric field effect. (a) The schematic ferroelectric field effect on J_{ex}. For $P_\uparrow$ state, the positive bound charge on the NiO/PMN–PT interface induce electron doping into NiO layer, which possesses strong J_{ex}. For $P_\downarrow$ state, negative bound charge on the NiO/PMN–PT interface induce hole doping into NiO layer, which possesses weak J_{ex}. The yellow arrows are ferroelectric polarizations. The symbols "+" and "−" with circles denote positive or negative bound charge, while those without circles denote hole/electron doping. (b) the DFT calculated J_{ex} as a function of the number of charge per u.c. (N) for electron or hole doping.

reorientation at low temperature [40, 41]. Furthermore, the XMLD signal from the $P_\downarrow$ state shows a similar non-monotonic trend but remains less than the XMLD signal magnitude from the $P_\uparrow$ state. This trend aligns with the AHE results in Figure 1(d), showing that the AFM order strength of $P_\downarrow$ state is weaker than that in $P_\uparrow$ state, which is also consistent with the reported correlation between AHE and AFM order strength in AFM conductors [6, 11, 42].

As a relaxor ferroelectric with significant piezoelectric effect, after applying reverse E_{gate}, the observed non-volatile control of AHE could be a combination of ferroelectric polarization switching and piezoelectric strain effect. The PMN–PT has a rhombohedral crystal structure, with the ferroelectric polarization of PMN–PT along ⟨111⟩ directions in pseudo-cubic notation [3, 43]. Thus, a critical reverse E_{gate} applied along the [001] direction can lead to 71°, 109° and 180° switching of ferroelectric polarization [44]. Although saturation E_{gate} favors 180° switching and volatile in-plane strain after removing the electric field, minor 71° or 109° switching can also remain and induce non-volatile strain that modulates the AFM order [45]. To clarify this issue, we measured the in-plane piezoelectric strain (ε) by using a strain gauge with continuous measurements on PMN–PT(100) substrate, see schematic diagram in Figure 3(a). The in-plane piezoelectric strain as a sweep E_{gate} along the [001] direction is displayed in Figure 3(b), showing a butterfly-shaped strain hysteresis loop with an asymmetry component. By defining the piezoelectric strain coefficient $\gamma = |d\varepsilon/dE_{gate}|$, we found the $\gamma_\uparrow = 0.0063$ % cm/kV for $P_\uparrow$ state, and $\gamma_\downarrow = 0.0058$ % cm/kV for $P_\downarrow$ state, respectively. Two non-volatile states with in-plane strain about −0.01% corresponding to $P_\uparrow$ state and about 0% corresponding to $P_\downarrow$ state were observed after removing E_{gate}. Next, to clarify the dominant effect in the non-volatile control of AFM order, we studied the piezoelectric response of AHE. The polarization is held upward for $P_\uparrow$ state and downward for $P_\downarrow$ state, respectively, and the E_{gate} is applied *in-situ* to the device up to ±4 kV/cm; see detailed raw data in Figure S9, Supplementary Materials. The results are shown in Figure 3(c) and Figure 3(d), displaying similar magnitude of magnetoelectric coupling coefficient $\beta = dR_{AHE}/dE_{gate}$ for both states. We found $\beta_\uparrow = 0.31$ mΩ cm/kV for $P_\uparrow$ state and $\beta_\downarrow = 0.44$ mΩ cm/kV for $P_\downarrow$ state. The increase of in-plane compressive strain gives rise to enhancement of R_{AHE}, which can be understood as the enhancement of AFM interaction J_{ex} by reducing interatomic spacing [42]. However, the magnitude of R_{AHE} of $P_\downarrow$ state is always lower than that of $P_\uparrow$ state in the range of applied E_{gate}. Considering the strain difference of about 0.01% between $P_\uparrow$ and $P_\downarrow$, the pure modulation of R_{AHE} originates from the remnant strain can be calculated through $\Delta R_{AHE}^{strain} = \frac{dR_{AHE}}{d\varepsilon}\Delta\varepsilon = \frac{dR_{AHE}}{dE_{gate}} \cdot \frac{dE_{gate}}{d\varepsilon}\Delta\varepsilon = \beta/\gamma \cdot \Delta\varepsilon$. Using the coefficiencies from experimental results, we estimated the ΔR_{AHE}^{strain} is about 0.63±0.14 mΩ, which can only contribute to about 25% of the non-volatile modulation of the R_{AHE} in Figure 1(c). Thus, in our system, the field effect imposed by ferroelectric polarization of PMN–PT mainly contributes to the non-volatile control of AFM order strength and corresponding R_{AHE}.

Due to the bound charge carried by ferroelectric polarization, electron/hole doping into the ultrathin NiO layer could happen for $P_\uparrow/P_\downarrow$ states [46–48]. In correlated

magnetic materials, this doping usually results in modulation of $J_{\rm ex}$ [49], as schematically shown in Figure 4(a). To qualitatively understand the impact of hole/electron doping on $J_{\rm ex}$ in the NiO layer, we conducted theoretical calculations based on density functional theory (DFT) to investigate J_{ex}. The number of doping charge per unit cell (N) for either electron or hole doping is simply estimated by $N = PV_0/de \approx$ 0.07, where $P \approx 20$ μC/cm^2 is the magnitude of ferroelectric polarization, V_0 is the volume of the NiO unit cell, $d \approx$ 1.2 nm is the thickness of the NiO layer, and e is the electron charge. Thus, we calculated $J_{\rm ex}$ considering N from 0 to 0.1 with electron or hole doping. The NiO remains insulating according to the band structure, see details in Figure S10, Supplementary Materials. Without doping, $J_{\rm ex}$ is calculated to be about -9.3 meV, located in the reasonable range within previous theoretical studies [50, 51]. Furthermore, our DFT calculations revealed that both hole and electron doping in the NiO layer lead to a weakening of the $J_{\rm ex}$. However, this modulation depends on the type of doping and shows strong asymmetry, which has been intensively demonstrated in correlated materials [49, 52, 53]. The $J_{\rm ex}$ of electron doping is always larger than hole doping, giving rise to stronger AFM strength probed by larger AHE at RT (Figure 1), as well as a stronger XMLD signal (Figure 2). The DFT calculation is further supported by a Pt(3 nm)/NiO(4 u.c.)/PMN-PT control sample (see Figure S11 in Supplementary Materials), in which the nonvolatile modulation of AHE resistance is much smaller due to thicker NiO, aligning with the scenario of the ferroelectric field-effect.

Our results highlight that the AFM state can be effectively probed through interfacial effects using the AHE, despite the spin-independent nature of bulk AFMs that normally preserves spin degeneracy. Although demonstrated here with insulating NiO, similar phenomena could be extended to conducting AFMs through precise thickness control, opening new avenues for designing functional interface-engineered AFM devices [54, 55]. A possible asymmetric spin–orbit torque driven AFM switching may also emerge with an appropriate crystalline orientation under a piezoelectric strain–modulated energy barrier governed by the AFM strength [56].

III. CONCLUSION

In conclusion, we report the electric-field manipulation of AFM order in hybrid HM/AFMI heterostructures on PMN–PT substrate. By applying $E_{\rm gate}$, a non-volatile 33% control of $\sigma_{\rm AHE}$ is observed at RT. Using XMLD measurements, the modulation of $R_{\rm AHE}$ is ascribed to the control of AFM order. In addition, by monitoring the piezoelectric effect on $R_{\rm AHE}$, we conclude that the non-volatile control of $R_{\rm AHE}$ is mainly contributed by ferroelectric polarization of PMN–PT, which modulates the image charge screening effect from Pt for the enhancement or reduction of $J_{\rm ex}$. The DFT calculation shows the asymmetric $J_{\rm ex}$ dependence on the electron or hole doping induced by the ferroelectric field effect on the NiO layer. Our results may facilitate the development of AFM-based spintronic devices.

ACKNOWLEDGMENTS

We thank the staff at beamline BL07U of the Shanghai Synchrotron Radiation Facility (SSRF) for fruitful discussions and experimental assistance. L.W. acknowledges the support from the National Natural Science Foundation of China (Grant No. 52102131). Y.-H.L acknowledges the support from the Basic Science Center Project of the National Natural Science Foundation of China (Grant No. 52388201). D.Y. acknowledges the support from National Natural Science Foundation of China (Grant No. 52250418).

DATA AVAILABILITY

The data that support the findings of this study are available from the corresponding author upon reasonable request.

[1] V. Baltz, A. Manchon, M. Tsoi, T. Moriyama, T. Ono, and Y. Tserkovnyak, Antiferromagnetic spintronics, Rev. Mod. Phys. **90**, 015005 (2018).
[2] J. Han, R. Cheng, L. Liu, H. Ohno, and S. Fukami, Coherent antiferromagnetic spintronics, Nat. Mater. **22**, 684 (2023).
[3] H. Yan, Z. Feng, S. Shang, X. Wang, Z. Hu, J. Wang, Z. Zhu, H. Wang, Z. Chen, H. Hua, W. Lu, J. Wang, P. Qin, H. Guo, X. Zhou, Z. Leng, Z. Liu, C. Jiang, M. Coey, and Z. Liu, A piezoelectric, strain-controlled antiferromagnetic memory insensitive to magnetic fields, Nat. Nanotechnol. **14**, 131 (2019).
[4] Y. Chai, Y. Liang, C. Xiao, Y. Wang, B. Li, D. Jiang, P. Pal, Y. Tang, H. Chen, Y. Zhang, H. Bai, T. Xu, W. Jiang, W. Skowroński, Q. Zhang, L. Gu, J. Ma, P. Yu, J. Tang, Y.-H. Lin, D. Yi, D. C. Ralph, C.-B. Eom, H. Wu, and T. Nan, Voltage control of multiferroic magnon torque for reconfigurable logic-in-memory, Nat. Commun. **15**, 5975 (2024).
[5] Y. Liang, D. Jiang, Y. Chai, Y. Wang, H. Chen, J. Ma, P. Yu, D. Yi, and T. Nan, Observation of magnon spin transport in $BiFeO_3$ thin films, Adv. Funct. Mater. **34**, 2308944 (2024).
[6] S. Nakatsuji, N. Kiyohara, and T. Higo, Large anomalous Hall effect in a non-collinear antiferromagnet at room

temperature, Nature **527**, 212 (2015).
[7] A. K. Nayak, J. E. Fischer, Y. Sun, B. Yan, J. Karel, A. C. Komarek, C. Shekhar, N. Kumar, W. Schnelle, J. Kübler, C. Felser, and S. S. P. Parkin, Large anomalous Hall effect driven by a nonvanishing Berry curvature in the noncolinear antiferromagnet Mn_3Ge, Sci. Adv. **2**, e1501870 (2016).
[8] Y. Zhou, C. Guo, C. Wan, X. Chen, X. Zhou, R. Zhang, Y. Gu, R. Chen, H. Wu, X. Han, F. Pan, and C. Song, Current-induced in-plane magnetization switching in a biaxial ferrimagnetic insulator, Phys. Rev. Appl. **13**, 064051 (2020).
[9] Y. Cheng, S. Yu, M. Zhu, J. Hwang, and F. Yang, Electrical switching of tristate antiferromagnetic Néel order in $\alpha-Fe_2O_3$ epitaxial films, Phys. Rev. Lett. **124**, 027202 (2020).
[10] H. Chen, Q. Niu, and A. H. MacDonald, Anomalous Hall effect arising from noncollinear antiferromagnetism, Phys. Rev. Lett. **112**, 017205 (2014).
[11] N. Nagaosa, J. Sinova, S. Onoda, A. H. MacDonald, and N. P. Ong, Anomalous Hall effect, Rev. Mod. Phys. **82**, 1539 (2010).
[12] Z. Feng, X. Zhou, L. Šmejkal, L. Wu, Z. Zhu, H. Guo, R. González-Hernández, X. Wang, H. Yan, P. Qin, X. Zhang, H. Wu, H. Chen, Z. Meng, L. Liu, Z. Xia, J. Sinova, T. Jungwirth, and Z. Liu, An anomalous Hall effect in altermagnetic ruthenium dioxide, Nat. Electron. **5**, 735 (2022).
[13] L. Šmejkal, J. Sinova, and T. Jungwirth, Beyond conventional ferromagnetism and antiferromagnetism: A phase with nonrelativistic spin and crystal rotation symmetry, Phys. Rev. X **12**, 031042 (2022).
[14] L. Šmejkal, J. Sinova, and T. Jungwirth, Emerging research landscape of altermagnetism, Phys. Rev. X **12**, 040501 (2022).
[15] Z. Zhou, X. Cheng, M. Hu, R. Chu, H. Bai, L. Han, J. Liu, F. Pan, and C. Song, Manipulation of the altermagnetic order in CrSb via crystal symmetry, Nature **638**, 645 (2025).
[16] Y. Wang, X. Zhou, C. Song, Y. Yan, S. Zhou, G. Wang, C. Chen, F. Zeng, and F. Pan, Electrical control of the exchange spring in antiferromagnetic metals, Adv. Mater. **27**, 3196 (2015).
[17] B. Huang, G. Clark, D. R. Klein, D. MacNeill, E. Navarro-Moratalla, K. L. Seyler, N. Wilson, M. A. McGuire, D. H. Cobden, D. Xiao, W. Yao, P. Jarillo-Herrero, and X. Xu, Electrical control of 2D magnetism in bilayer CrI_3, NNat. Nanotechnol. **13**, 544 (2018).
[18] Z. Liu, Z. Feng, H. Yan, X. Wang, X. Zhou, P. Qin, H. Guo, R. Yu, and C. Jiang, Antiferromagnetic piezospintronics, Adv. Electron. Mater. **5**, 1900176 (2019).
[19] X. Chen, X. Zhou, R. Cheng, C. Song, J. Zhang, Y. Wu, Y. Ba, H. Li, Y. Sun, Y. You, Y. Zhao, and F. Pan, Electric field control of Néel spin–orbit torque in an antiferromagnet, Nat. Mater. **18**, 931 (2019).
[20] T. Higo, K. Kondou, T. Nomoto, M. Shiga, S. Sakamoto, X. Chen, D. Nishio-Hamane, R. Arita, Y. Otani, S. Miwa, and S. Nakatsuji, Perpendicular full switching of chiral antiferromagnetic order by current, Nature **607**, 474 (2022).
[21] H. Tsai, T. Higo, K. Kondou, T. Nomoto, A. Sakai, A. Kobayashi, T. Nakano, K. Yakushiji, R. Arita, S. Miwa, Y. Otani, and S. Nakatsuji, Electrical manipulation of a topological antiferromagnetic state, Nature **580**, 608 (2020).
[22] X. Chen, T. Higo, K. Tanaka, T. Nomoto, H. Tsai, H. Idzuchi, M. Shiga, S. Sakamoto, R. Ando, H. Kosaki, T. Matsuo, D. Nishio-Hamane, R. Arita, S. Miwa, and S. Nakatsuji, Octupole-driven magnetoresistance in an antiferromagnetic tunnel junction, Nature **613**, 490 (2023).
[23] P. Qin, H. Yan, X. Wang, H. Chen, Z. Meng, J. Dong, M. Zhu, J. Cai, Z. Feng, X. Zhou, L. Liu, T. Zhang, Z. Zeng, J. Zhang, C. Jiang, and Z. Liu, Room-temperature magnetoresistance in an all-antiferromagnetic tunnel junction, Nature **613**, 485 (2023).
[24] P. Wadley, B. Howells, J. Železný, C. Andrews, V. Hills, R. P. Campion, V. Novák, K. Olejník, F. Maccherozzi, S. S. Dhesi, S. Y. Martin, T. Wagner, J. Wunderlich, F. Freimuth, Y. Mokrousov, J. Kuneš, J. S. Chauhan, M. J. Grzybowski, A. W. Rushforth, K. W. Edmonds, B. L. Gallagher, and T. Jungwirth, Electrical switching of an antiferromagnet, Science **351**, 587 (2016).
[25] C.-T. Chou, S. Ghosh, B. C. McGoldrick, T. Nguyen, G. Gurung, E. Y. Tsymbal, M. Li, K. A. Mkhoyan, and L. Liu, Large spin polarization from symmetry-breaking antiferromagnets in antiferromagnetic tunnel junctions, Nat. Commun. **15**, 7840 (2024).
[26] Y. Liang, L. Wu, M. Dai, Y. Zhang, Q. Zhang, J. Wang, N. Zhang, W. Xu, L. Zhao, H. Chen, J. Ma, J. Wu, Y. Cao, D. Yi, J. Ma, W. Jiang, J.-M. Hu, C.-W. Nan, and Y.-H. Lin, Significant unconventional anomalous Hall effect in heavy metal/antiferromagnetic insulator heterostructures, Adv. Sci. **10**, 2206203 (2023).
[27] T. Moriyama, Y. Shiratsuchi, T. Iino, H. Aono, M. Suzuki, T. Nakamura, Y. Kotani, R. Nakatani, K. Nakamura, and T. Ono, Giant anomalous Hall conductivity at the Pt/Cr_2O_3 Interface, Phys. Rev. Appl. **13**, 034052 (2020).
[28] Y. Ji, J. Miao, Y. M. Zhu, K. K. Meng, X. G. Xu, J. K. Chen, Y. Wu, and Y. Jiang, Negative spin Hall magnetoresistance in antiferromagnetic Cr_2O_3/Ta bilayer at low temperature region, Appl. Phys. Lett. **112**, 232404 (2018).
[29] Y. Cheng, S. Yu, M. Zhu, J. Hwang, and F. Yang, Evidence of the topological Hall effect in Pt/antiferromagnetic insulator bilayers, Phys. Rev. Lett. **123**, 237206 (2019).
[30] S. Altieri, M. Finazzi, H. H. Hsieh, M. W. Haverkort, H.-J. Lin, C. T. Chen, S. Frabboni, G. C. Gazzadi, A. Rota, S. Valeri, and L. H. Tjeng, Image charge screening: A new approach to enhance magnetic ordering temperatures in ultrathin correlated oxide films, Phys. Rev. B **79**, 174431 (2009).
[31] F.-Y. Zhu, J.-F. Cao, X.-Y. Meng, J.-Q. Li, R. Yu, Y.-M. Wang, S. Qiao, B. Zhao, M.-Z. Zhang, Z.-K. Liu, M.-X. Wang, Y. Wang, and R.-Z. Tai, Spatial- and spin-resolution ARPES and magnetism beamline at SSRF, Nucl. Sci. Tech. **35**, 130 (2024).
[32] X. Z. Chen, R. Zarzuela, J. Zhang, C. Song, X. F. Zhou, G. Y. Shi, F. Li, H. A. Zhou, W. J. Jiang, F. Pan, and Y. Tserkovnyak, Antidamping-torque-induced switching in biaxial antiferromagnetic insulators, Phys. Rev. Lett. **120**, 207204 (2018).
[33] T. Moriyama, K. Oda, T. Ohkochi, M. Kimata, and T. Ono, Spin torque control of antiferromagnetic mo-

ments in NiO, Sci. Rep. **8**, 14167 (2018).
[34] K. Cai, M. Yang, H. Ju, S. Wang, Y. Ji, B. Li, K. W. Edmonds, Y. Sheng, B. Zhang, N. Zhang, S. Liu, H. Zheng, and K. Wang, Electric field control of deterministic current-induced magnetization switching in a hybrid ferromagnetic/ferroelectric structure, Nat. Mater. **16**, 712 (2017).
[35] D. Alders, L. H. Tjeng, F. C. Voogt, T. Hibma, G. A. Sawatzky, C. T. Chen, J. Vogel, M. Sacchi, and S. Iacobucci, Temperature and thickness dependence of magnetic moments in NiO epitaxial films, Phys. Rev. B **57**, 11623 (1998).
[36] J. Stöhr, A. Scholl, T. J. Regan, S. Anders, J. Lüning, M. R. Scheinfein, H. A. Padmore, and R. L. White, Images of the antiferromagnetic structure of a NiO(100) surface by means of x-ray magnetic linear dichroism spectromicroscopy, Phys. Rev. Lett. **83**, 1862 (1999).
[37] Y. Z. Wu, Y. Zhao, E. Arenholz, A. T. Young, B. Sinkovic, C. Won, and Z. Q. Qiu, Analysis of x-ray linear dichroism spectra for NiO thin films grown on vicinal Ag(001), Phys. Rev. B **78**, 064413 (2008).
[38] I. Gray, T. Moriyama, N. Sivadas, G. M. Stiehl, J. T. Heron, R. Need, B. J. Kirby, D. H. Low, K. C. Nowack, D. G. Schlom, D. C. Ralph, T. Ono, and G. D. Fuchs, Spin Seebeck imaging of spin-torque switching in antiferromagnetic Pt/NiO heterostructures, Phys. Rev. X **9**, 041016 (2019).
[39] L. Baldrati, A. Ross, T. Niizeki, C. Schneider, R. Ramos, J. Cramer, O. Gomonay, M. Filianina, T. Savchenko, D. Heinze, A. Kleibert, E. Saitoh, J. Sinova, and M. Kläui, Full angular dependence of the spin Hall and ordinary magnetoresistance in epitaxial antiferromagnetic NiO(001)/Pt thin films, Phys. Rev. B **98**, 024422 (2018).
[40] J. Zhu, Q. Li, J. X. Li, Z. Ding, J. H. Liang, X. Xiao, Y. M. Luo, C. Y. Hua, H.-J. Lin, T. W. Pi, Z. Hu, C. Won, and Y. Z. Wu, Antiferromagnetic spin reorientation transition in epitaxial NiO/CoO/MgO(001) systems, Phys. Rev. B **90**, 054403 (2014).
[41] Y. Z. Wu, Z. Q. Qiu, Y. Zhao, A. T. Young, E. Arenholz, and B. Sinkovic, Tailoring the spin direction of antiferromagnetic NiO thin films grown on vicinal Ag(001), Phys. Rev. B **74**, 212402 (2006).
[42] Z. Q. Liu, H. Chen, J. M. Wang, J. H. Liu, K. Wang, Z. X. Feng, H. Yan, X. R. Wang, C. B. Jiang, J. M. D. Coey, and A. H. MacDonald, Electrical switching of the topological anomalous Hall effect in a non-collinear antiferromagnet above room temperature, Nat. Electron. **1**, 172 (2018).
[43] A. Chen, Y. Wen, B. Fang, Y. Zhao, Q. Zhang, Y. Chang, P. Li, H. Wu, H. Huang, Y. Lu, Z. Zeng, J. Cai, X. Han, T. Wu, X.-X. Zhang, and Y. Zhao, Giant nonvolatile manipulation of magnetoresistance in magnetic tunnel junctions by electric fields via magnetoelectric coupling, Nat. Commun. **10**, 243 (2019).
[44] L. Yang, Y. Zhao, S. Zhang, P. Li, Y. Gao, Y. Yang, H. Huang, P. Miao, Y. Liu, A. Chen, C. W. Nan, and C. Gao, Bipolar loop-like non-volatile strain in the (001)-oriented $Pb(Mg_{1/3}Nb_{2/3})O_3$-$PbTiO_3$ single crystals, Sci. Rep. **4**, 4591 (2014).
[45] Y. Ba, S. Zhuang, Y. Zhang, Y. Wang, Y. Gao, H. Zhou, M. Chen, W. Sun, Q. Liu, G. Chai, J. Ma, Y. Zhang, H. Tian, H. Du, W. Jiang, C. Nan, J.-M. Hu, and Y. Zhao, Electric-field control of skyrmions in multiferroic heterostructure via magnetoelectric coupling, Nat. Commun. **12**, 322 (2021).
[46] Y. Gu, Z. Zheng, L. Jia, S. Shi, T. Zhao, T. Zeng, Q. Zhang, Y. Zhu, H. Wang, and J. Chen, Ferroelectric control of spin-orbitronics, Adv. Func. Mater. **34**, 2406444 (2024).
[47] C. Song, B. Cui, F. Li, X. Zhou, and F. Pan, Recent progress in voltage control of magnetism: Materials, mechanisms, and performance, Prog. Mater. Sci. **87**, 33 (2017).
[48] M. Si, A. K. Saha, S. Gao, G. Qiu, J. Qin, Y. Duan, J. Jian, C. Niu, H. Wang, W. Wu, S. K. Gupta, and P. D. Ye, A ferroelectric semiconductor field-effect transistor, Nat. Electron. **2**, 580 (2019).
[49] L. M. Zheng, X. R. Wang, W. M. Lü, C. J. Li, T. R. Paudel, Z. Q. Liu, Z. Huang, S. W. Zeng, K. Han, Z. H. Chen, X. P. Qiu, M. S. Li, S. Yang, B. Yang, M. F. Chisholm, L. W. Martin, S. J. Pennycook, E. Y. Tsymbal, J. M. D. Coey, and W. W. Cao, Ambipolar ferromagnetism by electrostatic doping of a manganite, Nat, Commun, **9**, 1897 (2018).
[50] D. Ködderitzsch, W. Hergert, W. M. Temmerman, Z. Szotek, A. Ernst, and H. Winter, Exchange interactions in nio and at the NiO(100) surface, Phys. Rev. B **66**, 064434 (2002).
[51] I. de P. R. Moreira, F. Illas, and R. L. Martin, Effect of Fock exchange on the electronic structure and magnetic coupling in NiO, Phys. Rev. B **65**, 155102 (2002).
[52] E. M. Pärschke, K. Wohlfeld, K. Foyevtsova, and J. van den Brink, Correlation induced electron-hole asymmetry in quasi-two-dimensional iridates, Nat. Commun. **8**, 686 (2017).
[53] K. Segawa, M. Kofu, S. Lee, I. Tsukada, H. Hiraka, M. Fujita, S. Chang, K. Yamada, and Y. Ando, Zero-doping state and electron–hole asymmetry in an ambipolar cuprate, Nat. Phys. **6**, 579 (2010).
[54] L. Yang, Y.-Y. Jiang, X.-Y. Guo, S.-H. Zhang, R.-C. Xiao, W.-J. Lu, L. Wang, Y.-P. Sun, E. Y. Tsymbal, and D.-F. Shao, Interface-controlled antiferromagnetic tunnel junctions, Newton **1**, 100142 (2025).
[55] W.-M. Zhao, Y.-L. Liu, L. Yang, C. Tan, Y. Yang, Z. Zhu, M. Chen, T. Yan, R. Hu, J. Partridge, G. Wang, M. Tian, D.-F. Shao, and L. Wang, Collinear antiferromagnetic tunnel junctions implemented in van der Waals heterostructures (2025), arXiv:2507.12735.
[56] S.-S. Zhang, Z.-A. Wang, B. Li, W.-J. Lu, M. Tian, Y.-P. Sun, H. Du, and D.-F. Shao, Deterministic switching of the Néel vector by asymmetric spin torque (2025), arXiv:2506.10786.

Supplementary Materials

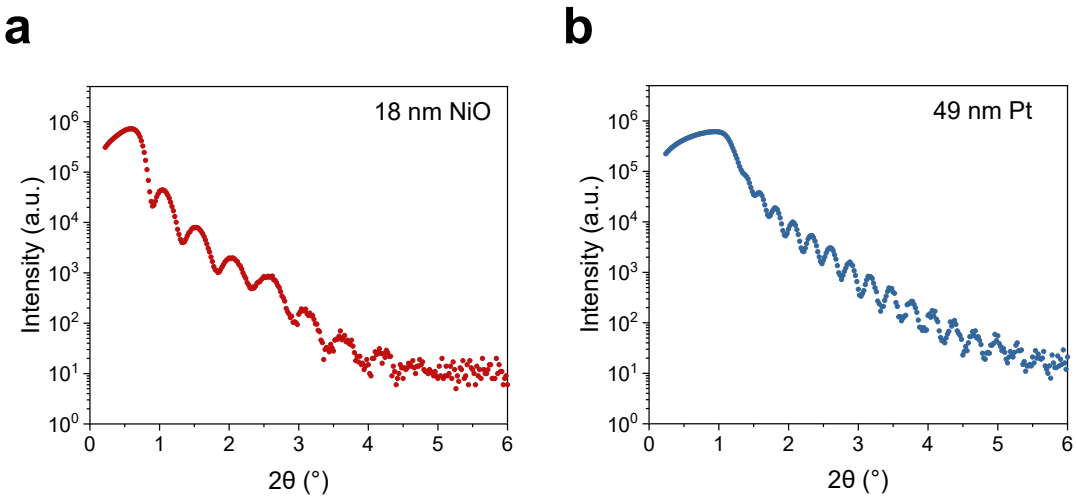

Figure S1. The XRR raw data of (a) 18 nm NiO and (b) 49 nm Pt.

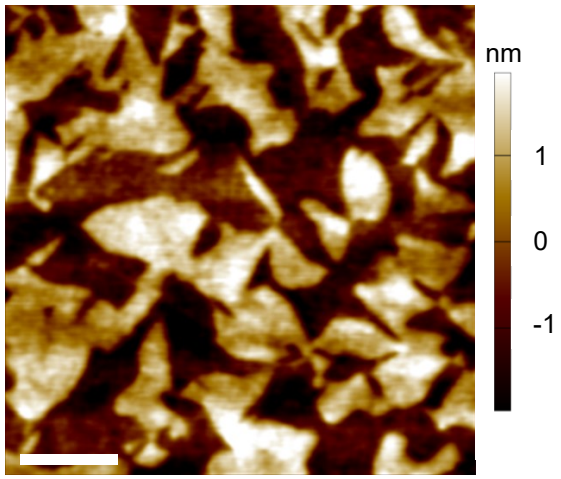

Figure S2. The atomic force microscopy image of Pt(3 nm)/NiO(3 u.c.)/PMN-PT heterostructure. The scale bar is 1 μm.

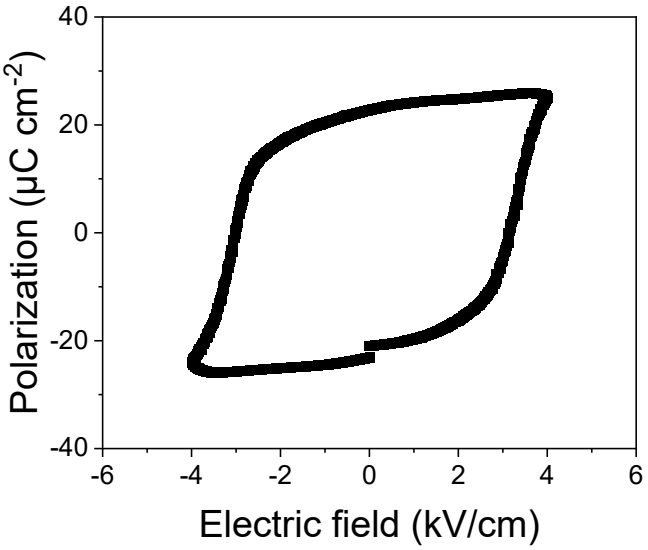

Figure S3. The polarization–electric field hysteresis loop of PMN–PT substrate.

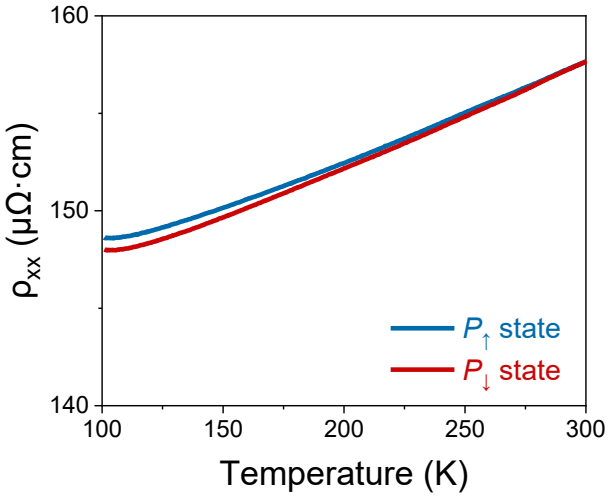

Figure S4. The temperature-dependent resistivity for $P_{\uparrow}$ state and $P_{\downarrow}$ state, respectively.

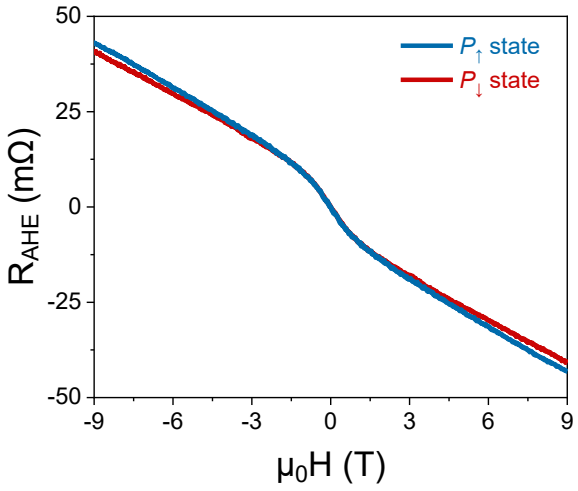

Figure S5. The raw data of AHE resistance as a function of out-of-plane magnetic field for $P_\uparrow$ state and $P_\downarrow$ state, respectively.

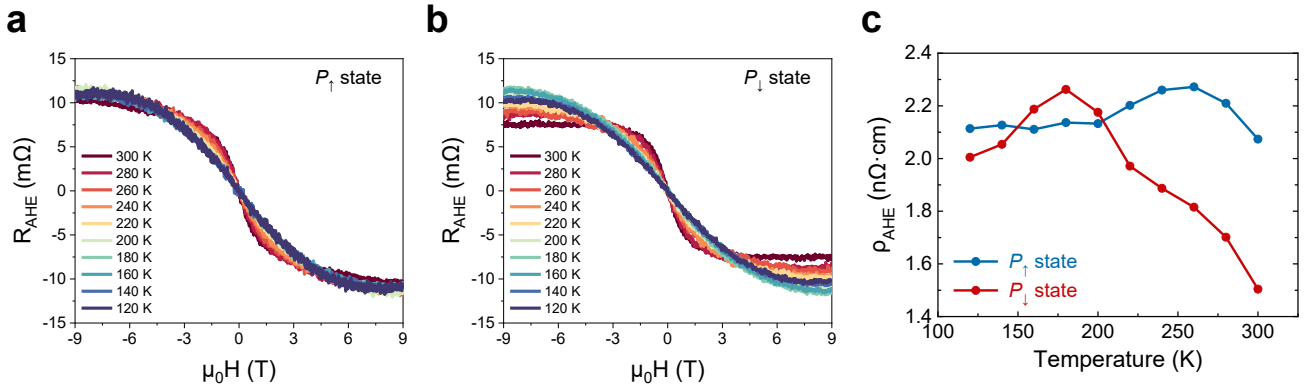

Figure S6. The AHE resistance under different temperature for (a) $P_\uparrow$ state and (b) $P_\downarrow$ state, respectively. The temperature dependent saturated R_{AHE} for both states are summarized in (c).

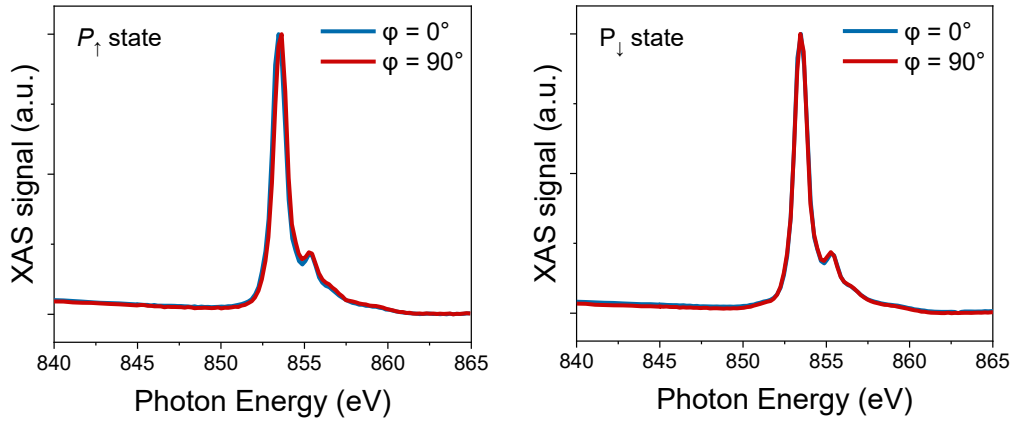

Figure S7. The Ni L_3 edge XAS results for $P_\uparrow$ state and $P_\downarrow$ states, respectively.

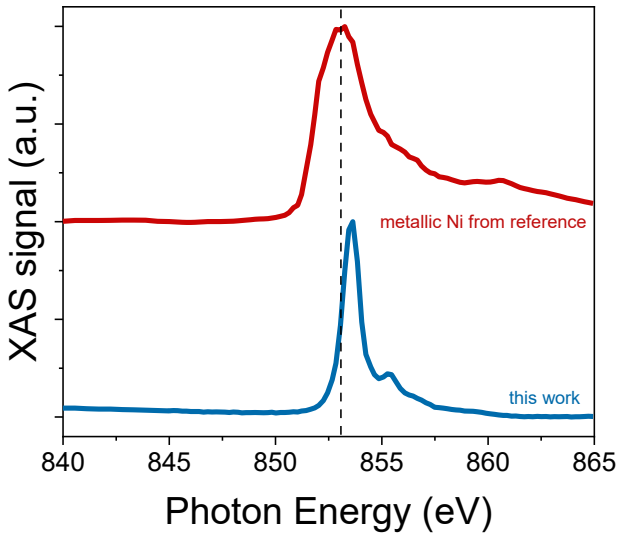

Figure S8. Ni L_3-edge spectra of metallic Ni [Phys. Rev. B 101, 115137 (2020)] and this work. The dash line indicates the peak position of metallic Ni, excluding the Ni defects in Pt for AHE.

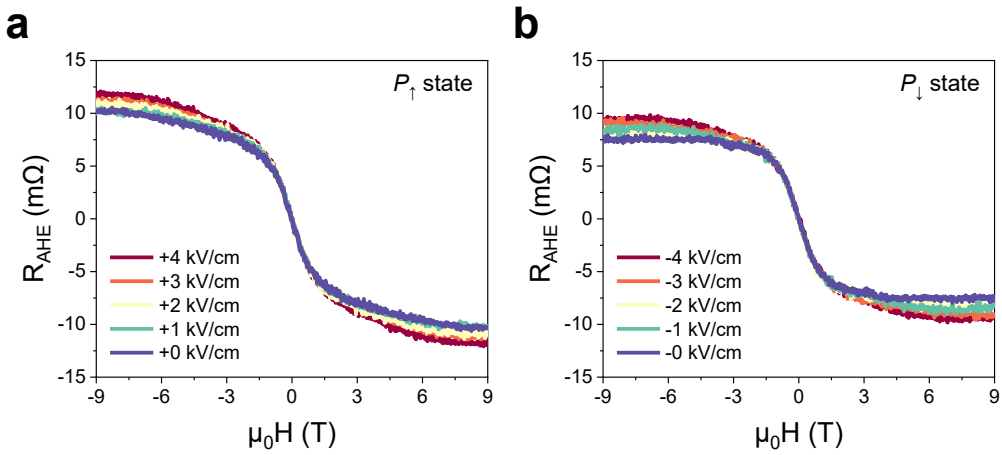

Figure S9. The AHE resistance under different E_{gate} for (a) $P_\uparrow$ state and (b) $P_\downarrow$ state, respectively.

The DFT calculation of J_{ex} in electron/hole doped NiO

The DFT calculation is performed using the Vienna *Ab initio* Simulation Package (VASP). The projector-augmented-wave (PAW) pseudopotential was utilized to treat the core electrons. The Perdew–Burke–Ernzerhof (PBE) functional, based on the generalized gradient approximation (GGA) for exchange-correlation, was chosen to simulate the electron interactions. The cutoff energy is set to 450 eV for all calculations. The Brillouin zone is sampled by a Monkhorst-Pack $4 \times 4 \times 4$ k-point mesh. To simplify the calculation, we only calculated the nearest exchange interaction between Ni atoms, expressed as J_{ex}. The schematic of the NiO primary unit cell is shown in Figure S8(a), as the rhombohedral unit cell vectors are given as $(1, 1/2, 1/2)_a$, where $a = 4.2$ Å. For each individual Ni that couples to the nearest Ni, the exchange coupling energy is expressed as $J_{ex}\mathbf{S}_1 \cdot \mathbf{S}_2$, where the magnitude of $\mathbf{S}_{1,2}$ equals 1 for Ni^{2+}. Thus, our strategy is to calculate the energy of AFM NiO (E_{AFM} where $J_{ex} < 0$), as well as the energy of ferromagnetic (FM) NiO (E_{FM} where $J_{ex} > 0$). The density of states (DOS) for AFM NiO and FM NiO are shown in Figure S8(b) and Figure S8(c) with a certain band gap, indicating that both are insulators. However, the band gap of FM NiO is narrower than that of AFM NiO. By determining the energy difference between AFM and FM NiO, represented by $\Delta E = E_{AFM} - E_{FM}$ and dependent on the number of charges per unit cell (N) as illustrated in Figure S8(d), we can subsequently compute the exchange interaction $J_{ex} = \Delta E/(24S^2)$.

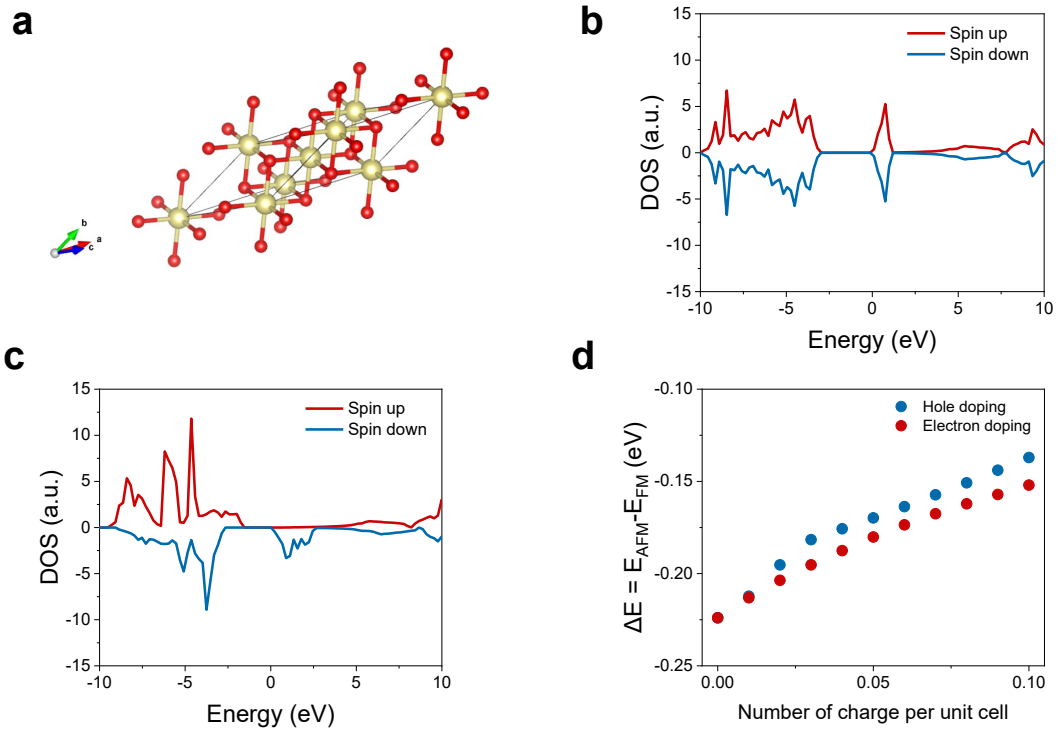

Figure S10. The details of DFT calculation. (a) The schematic of primary unit cell of NiO for DFT calculation. Only two Ni atoms are contained. The yellow balls are Ni atoms, red balls are oxygen atoms. (b) The calculated DOS as a function of energy of AFM NiO. (c) The calculated DOS as a function of energy of FM NiO. (d) The calculated ΔE as a function of number of charge per unit cell.

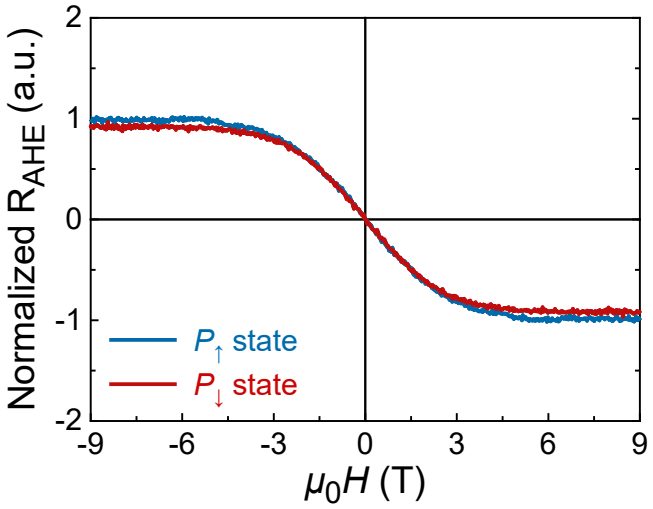

Figure S11. Normalized AHE resistance for the $P_\uparrow$ and $P_\downarrow$ states in a Pt(3 nm)/NiO(4 u.c.) heterostructure on a PMN-PT substrate.